ELSEVIER

Polymer 41 (2000) 7735–7747

polymer

Investigation of the nanofibrils of silk fibers

S. Putthanarat[a,*], N. Stribeck[b], S.A. Fossey[c], R.K. Eby[a], W.W. Adams[d]

[a]*Department of Polymer Science, The University of Akron, Akron, OH 44325-3909, USA*
[b]*Institut f. Technische und Makromoleculare Chemie, Universität, Hamburg 20146, Germany*
[c]*Natick Research, Development, and Engineering Center, US Army, Natick, MA 01760-5020, USA*
[d]*Air Force Research Laboratory, Materials and Manufacturing Directorate, AFRL/ML, WPAFB, OH 45433-7734, USA*

Dedicated to the memory of A. Keller, a colleague for more than three decades.

Received 19 August 1999; received in revised form 26 October 1999; accepted 1 November 1999

Abstract

Silk from 3-molted, 4-molted and sex-limited *Bombyx mori*, *Antheraea pernyi* and *Antheraea yamamai* have been investigated using Atomic Force Microscopy and Low Voltage High Resolution Scanning Electron Microscopy. Nanofibrils, bundles of nanofibrils, helical features and a layered structure with a cross angle between nanofibrils in different layers were observed for all silks. Similar log-normal distributions of fibril widths were obtained from all silks with the geometric mean fibril widths covering the range of 90–170 nm. There is no correlation of the fibril width with the fiber size from different types of silkworm. Similar normal distributions of cross angles were observed in 30% of the images with the arithmetic means covering the range of 30–50°. There is an apparent correlation of cross angle with fiber size. The larger fibers for which the crystals are primarily alanine exhibit a greater average cross angle, 46°, than do those of the smaller fibers for which the crystals are primarily alanine and glycine, 36°. Initial wide angle X-ray diffraction measurements on a single fiber of *A. pernyi* are consistent with the fraction of fibrils at different cross angles being 28%. A simplified computer calculation method and molecular modeling were used in a search for packing angles which minimize the interaction energy of packing between beta sheets. Initial results revealed no definitive evidence of epitaxy to account for the cross angles. It is proposed that a multifibrillar fiber offers a number of mechanical advantages over a solid fiber with the same cross sectional area.

Keywords: Silk; Nanofibrils; Atomic Force Microscopy

1. Introduction

Synthetic polymers tend to form nanofibrils under many conditions. Mechanical deformation of: polystyrene dissolved in evaporating benzene [1]; single crystals of polyethylene [2]; pellets of compressed virgin polytetrafluoroethylene molding powder [3]; and amorphous polymers which craze [4] produces nanofibrils. Solution crystallization under shear flow [5], extensional flow [6] and high electric field (electrospinning) [7] yields similar fibrils. Nanofibrils are formed during the coagulation of fibers spun by the dry-jet wet process from solutions of lyotropic rigid polymers, such as poly (*p*-phenylene benzo-bisthiazole) [8]. Thermotropic polymers spun from the melt also exhibit nanofibrils [9] as do "gel spun" fibers [10]. Polymerization of ethylene in an array of parallel nanoreactors produces nanofibrils [11]. The poly(2-cinnamonylethyl methacrylate) (PCEMA) blocks of a PS-*b*-PCEMA copolymer segregate in bulk films. When annealed at 110°C the PCEMA block form cylinders which can be crosslinked by UV photolysis. Subsequent dissolution of the PS in THF or toluene yields nanofibrils with a PCEMA core and a PS shell [12].

Naturally produced materials such as the "grown" fibers of keratins [13], cellulosics [14] and collagens [15] also exhibit nanofibrils, as do silks which are "spun". Various spider silks have been investigated and found to be nanofibrillar. An early observation of fibers from the cylindrical gland of *Polencia producta* showed longitudinal bands which were not observed throughout the fiber [16]. Various enzyme and solvent treatments of fibers from the cylindrical gland of the orb weaver *Argiope aurantia* exposed more distinct nanofibrils [17]. These were confirmed by Transmission Electron Microscopy (TEM) examination of ultramicrotomed cross sections of the fibers. Scanning Electron Microscopy (SEM) and Atomic Force Microscopy (AFM)

* Corresponding author. Tel.: +1-330-972-8282; fax: +1-330-972-6581.
E-mail address: sirina@polymer.uakron.edu (S. Putthanarat).

0032-3861/00/$ - see front matter
PII: S0032-3861(00)00036-7

examination of the abraded surfaces of dragline silk from *Nephila clavipes* showed nanofibrillar striations, but these were not considered definitive because of the possible effects of the abrasion process on the oriented fibers [18]. However, small angle X-ray scattering (SAXS) measurements have been shown to be consistent with the presence of nanofibrils in the silk from *N. clavipes* [19]. SEM observations also were made on the abraded dragline silk of *Nephila clavata* [20]. AFM observations of cryomicrotomed sections of the dragline silk from *N. clavipes* revealed nanofibrils with a pleated structure arranged in concentric cylindrical cores [21]. Optical and electron microscopical observations of urea-supercontracted dragline silk of *Nephila madagascariensis* also showed a nanofibrillar tube. The fibrils appeared to be helically wound about the tube [22]. Nanofibrils have been produced by electrospining a solution of the dragline silk of *N. clavipes* [23].

Nanofibrils also have been observed in silk from the silkworms of *Antheraea pernyi*, *Anaphe moloneyi*, *Antheraea assama* and *Bombyx mori*. Early observations were made with fragments produced by a blender or ultrasound and were not always definitive [24–27]. Other observations were made with partially digested, dissolved, regenerated and swollen fibers as well as precipitated material from the silk gland of *B. mori* [28–30]. Longitudinal striations were observed on degummed *A. assama* [31]. Aggregates of single crystals formed from a solution of the Cp fraction of *B. mori* exhibited a short twisted fibrillar-like structure [32]. Nanofibrils have been electrospun from a solution of silk from *B. mori* [23]. Our earlier investigations with an AFM of peeled fibers revealed an interior morphology of nanofibrils in a layered structure. The nanofibrils on different layers crossed [33,34]. Also, our SAXS measurements have been shown to be consistent with the presence of nanofibrils in the silk of *B. mori* [19].

Since these nanofibrils no doubt play a role in determining the attractive mechanical properties [19] of silks and are relevant to other aspects of the structure, they warrant further characterization. This article reports a more detailed investigation of the nanofibrils of silkworm silks than those reported earlier. The fibril widths are measured in statistically more significant detail for silks from a variety of silkworms that produce fibers of different sizes. The presence of cross angles for nanofibrils on different layers [33,34] is confirmed and the angles are measured for the different silks. In addition, both width and angle measurements are made at the ends of the 1 km long single fiber which is wider on the outside and narrower on the inside of the cocoon [35]. Wide-angle X-ray diffraction (WAXD) measurements are made on a single fiber of *A. pernyi* in an initial attempt to resolve the relative amounts of the nanofibrils oriented parallel to the fiber axis and at a cross angle. Molecular modeling computations of the packing energy are made for the beta sheet crystals at different cross angles in an initial attempt to seek possible low-energy angles. EpiCalc, a simplified computer modeling calculation, also is used to seek possible favorable packing angles [36].

2. Experimental

2.1. Materials

Cocoon silks of 4-molted, 3-molted and sex-limited *B. mori* were used as well as the wild silks *Antheraea yamamai* (Japanese Tussah) and *A. pernyi* (Chinese Tussah). The 3-molted silkworm is induced to produce silk at a younger age by the administration of an anti-juvenile hormone [30]. Because it is younger, its spinnerette is smaller and it generally produces finer silk. The sex-limited silkworm is a genetic variation. The female produces cocoons of a different color than the male. Thus, the silk of the two sexes can be separated easily. Silk produced by the female is used in this work.

2.2. Sample preparation

The raw silks of the various *B. mori* cocoons were reeled from water at about 45°C after having been placed in a series of hotter and cooler water for a few minutes each to soften the sericin [37]. The sericin was removed (degumming) by washing the fibers for 30 min in a 1 wt% solution of Marseille soap and 0.5 wt% of Na_2CO_3 in water at about 96°C, followed by rinsing with deionized water. The process was repeated several times with fresh solutions at successively lower temperatures. For the measurements at both ends of the single cocoon fiber of 4-molted *B. mori*, the raw silk was reeled continuously and separated into segments every 112.5 m. The fibers from the outer and inner parts were washed twice with a solution of higher concentration (2 wt% of Marseille soap and 0.5 wt% of Na_2CO_3) for 40 min followed by rinsing with water and then with deionized water. The raw and degummed silks of *A. yamamai* and *A. pernyi*, which are more difficult to produce, were obtained from a laboratory abroad. All the silks were stored in the dark and under vacuum at room temperature in order to avoid degradation.

Peeling the silk fibers to expose the internal morphology was accomplished by a process of several steps. First, the degummed fiber was mounted on a glass slide with two-sided adhesive tape. Then, it was covered with a 3 wt% solution of collodion in amyl acetate and the solvent was allowed to evaporate leaving the fiber embedded in the substrate. The system was placed in an optical microscope and a razor blade was used to cut partially through perpendicular to the fiber axis. The fiber was peeled by slowly removing the mobile (upper) section with tweezers. Since the depth of the cut was difficult to control, it is likely that different depths were sampled in different peelings. The freshly exposed surface was used for AFM imaging by mounting it on a sample holder with a thermoplastic wax.

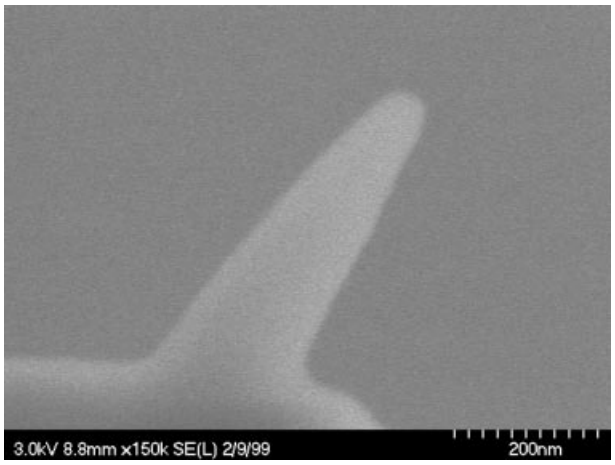

Fig. 1. LVHRSEM image of a microtip for the AFM.

For SEM imaging, the peeled sections were attached on a sample holder with a touch of silver paste.

2.3. Atomic force microscopy

An optical lever type AFM, TopoMetrix 2010, was used in the repulsive mode at ambient conditions. Images were obtained with a constant force of approximately 10^{-10}–10^{-9} N. A seven micron scanner was used for most of the images. For most of the images, 200–500 data points were taken for each line scan with an equal number of lines being taken. A line scan frequency of 1–3 Hz was used. For larger scale displacement of the sample, use was made of a coarser translator on which the scanner is mounted. The widths of the nanofibrils were measured on the profiles of the AFM images with software built into the operating system. These measurements are subject to some uncertainty if the profiles of the adjacent fibrils are not symmetric about their interface. An effort was made to avoid measuring those widths involving such an interface. Such errors can be reduced somewhat and the resolution improved by using a fine AFM tip.

2.4. Scanning electron microscopy

The SEM images were made with low voltage high resolution scanning electron microscopes (LVHRSEM). A Hitachi S-4700 was used to image the AFM tip at 3 keV without a conductive coating. The tip consisted of a microtip, with an aspect ratio of approximately 10:1, mounted on a "standard" pyramidal tip. The end of the microtip had a radius a little larger than 20 nm (Fig. 1). A Hitachi S-900 was used to image the silk. It was operated at 1–2 keV and required a 50 Å sputter coating of tungsten on the fiber samples to minimize sample charging.

2.5. Wide angle X-ray diffraction

WAXD measurements were made in an attempt to resolve the relative amounts of the nanofibrils oriented parallel to the fiber axis and at a cross angle. A single filament was examined to resolve the intrinsic orientation distribution of the crystallites in the fibril, since orientation data from filament bundles are smeared due to misorientation among the individual filaments. The measurements were performed on *A. pernyi* silk because it is the largest fiber and also has the largest average cross angle. The Deutsches Elektronen-Synchroton was used in order to shorten the required exposure time for the very fine fiber [38]. Even so, a 5 h total exposure was required. Repeat measurements during the 5 h showed no evidence of degradation. Detector efficiency was recorded separately. The data were corrected for background scatter. To reduce the noise, the data were integrated in two theta and averaged for the number of pixels involved. Thereafter, the analysis of the azimuthal spread of the equatorial peaks was carried out. Analysis of the diffraction patterns was performed using PV-Wave software.

2.6. Computational modeling

Initial computational modeling of the low-energy epitaxial packing angles for silk crystals was attempted with a simplified potential function embodied in the EpiCalc software [36]. The software searches for commensurate, incommensurate and coincident arrangements of two crystals. It accepts two-dimensional lattice parameters for the existing crystal substrate and the overlayer crystal. Both crystals were given the unit cell dimensions of the *ac* and *bc* faces of the beta sheet crystals [39–41]. To allow for cell distortions in the overlayer [36,42], a grid search in the cell dimensions of the overlayer was carried out in 0.01 Å steps over a range of approximately ± 1 and $\pm 2\%$ of the two dimensions, respectively. The unit cell angle was varied from 88 to 92° with an increment of 0.01°. The angle of relative orientation of the overlayer with respect to the substrate was stepped in 0.5° increments from 5–60° which covers more than the range of the experimentally observed cross angles. Angles smaller than 5° were encompassed in the 0° minimum associated with perfect alignment of the two crystals. To avoid mathematical artifacts in the calculation an overlayer of approximately 25×25 unit cells was used.

Since the crystals of silks are relatively small perpendicular to the molecular axis [27,43,44], molecular modeling calculations also were used in an initial effort to determine the excess interaction energy as a function of the relative orientation angle for a smaller overlayer and a larger substrate of β crystals. A model of the crystal of a "semi-finite" β-sheet, comprising four sheets each containing ten antiparallel molecules was developed. A "finite" single overlayer sheet of five antiparallel molecules was placed on top of the crystal at a series of orientations. Each molecule of the crystal and the sheet comprised five residues of one alanine and one glycine. Thus, the size of the overlayer is closer to the size that might be expected for a nucleating crystal. The hydrogen bonds in the crystal and sheet are parallel to the interface of the sheet and the crystal. The

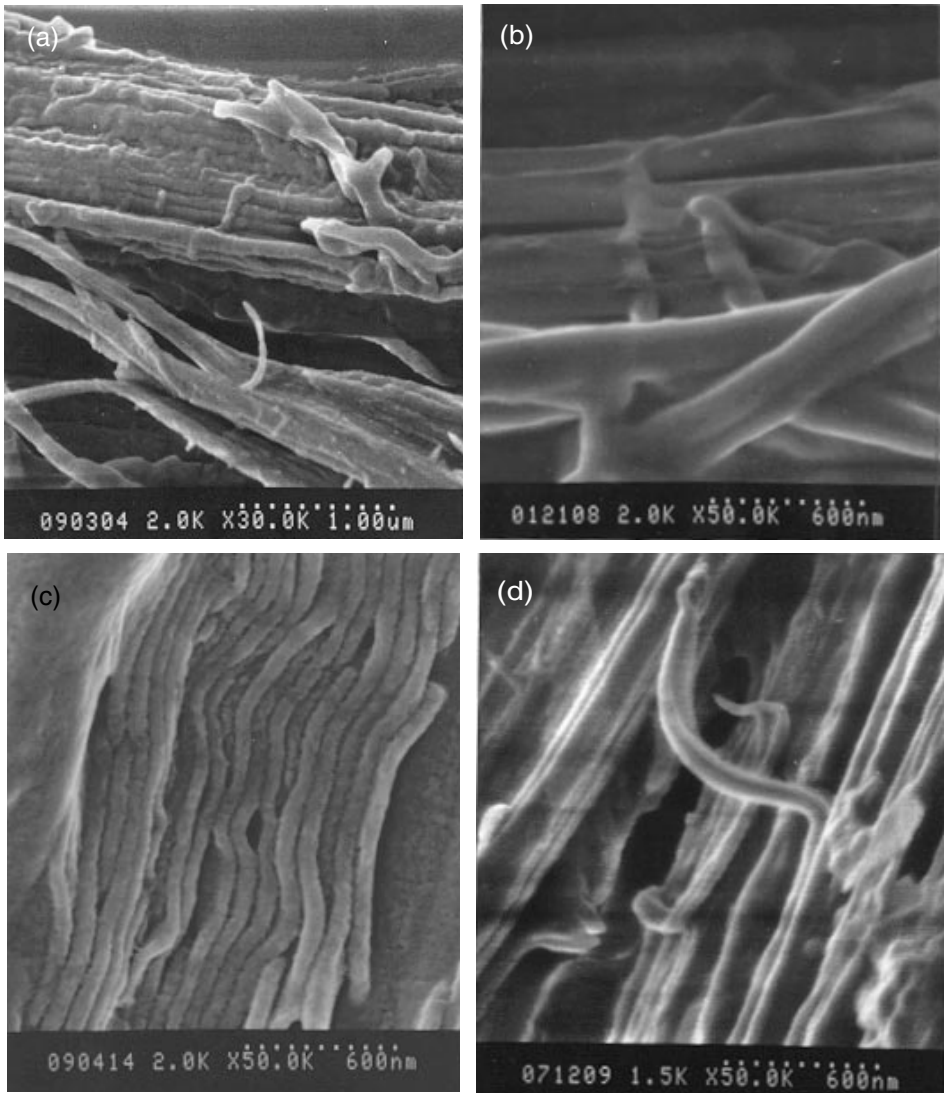

Fig. 2. LVHRSEM images of peeled silks: (a) *A. pernyi* at 2.0 keV; (b) *A. yamamai* at 2.0 keV; (c) 4-molted *B. mori* at 2.0 keV; and (d) 3-molted *B. mori* at 1.5 keV.

packing of four different combinations of single sheet and crystal were investigated.

Structure I: a crystal and an overlayer sheet of the polar-antiparallel β-structure of *B. mori* [39] with the alanine faces of each interacting.
Structure II: a crystal and an overlayer sheet of the polar-antiparallel β-structure of *B. mori* [39] with the glycine faces of each interacting.
Structure III: an overlayer sheet of the polar-antiparallel β-structure [39] with the alanine face interacting with a crystal of the antipolar-antiparallel β-structure [45] of *B. mori.*
Structure IV: a crystal and an overlayer sheet of the anti-polar-antiparallel β-structure of *B. mori* [45].

For each structure, seven orientations of the overlayer sheet corresponding to relative angles of 0, 15, 30, 45, 60, 75 and 90° were chosen. The crystal and the sheet were placed with their hydrogen-bonded surfaces parallel to one another. The initial perpendicular distance was selected so that the sheet and the crystal were closely spaced, while ensuring the absence of atom overlapping. This selection greatly reduced computation time. The energy minimization was carried out using Discover 3.0 of the MSI/Biosym software. The CVFF force field was used. The molecular variables of the "bottom" three sheets were constrained but those of the fourth sheet of the crystal and the overlayer sheet were not. For Structure I, the minimization also was carried out with the molecular variables of all the sheets being unconstrained. The minimization procedures used the conjugate gradient method with 10,000–15,000 iterations to determine the energy minima. If the systems did not converge, 20,000–1,000,000 iterations were used.

3. Results and discussion

3.1. Morphological observations

Fig. 2 shows representative LVHRSEM images of the interior surface exposed by peeling. All the silks exhibited nanofibrils, which are sometimes assembled into larger structures. Irregular features such as loose fibrils from the deformation also can be seen. These are not seen so clearly in the AFM images, presumably because the tip pushes them aside.

Very many AFM observations of the silk from 4-molted *B. mori* confirmed our earlier observations [33,34]. The degummed exterior surface exhibited somewhat irregular nanofibrils (Fig. 3a). For all the AFM images presented, the fiber axis is approximately parallel to the right-hand edge. The surface exposed by peeling exhibited relatively long and straight nanofibrils. They sometimes assembled into larger structures and sometimes exhibited helical features (Fig. 3b). The latter are probably related to the many possible conformations of β-sheet [46]. A layered structure also was observed with the fibrils on one layer crossing those on the next layer in a quaternary structure (Fig. 3c). Further, similar features are found in the four other silks examined (Figs. 4–6). Crossing fibrils were observed in about 30% of the AFM images for all the silks with some rotations being clockwise and some counterclockwise with respect to the fiber axis.

3.2. Fibril widths

Fig. 7 shows the width distribution of fibrils based on measurements of more than one hundred images of peeled, 4-molted *B. mori* fibers. The distributions are very similar for all the other peeled silks as well as the degummed silks [47]. Because of the asymmetry of the distribution in Fig. 7, Gaussian statistics do not apply. Fig. 8, which has a logarithmic dimension scale, exhibits a more nearly normal distribution. The arithmetic-mean and geometric-mean nanofibril widths for all the silks are summarized in Table 1. The arithmetic-mean fiber "diameters" are also given. They are somewhat difficult to measure because of the irregular triangular cross sections of the fibers [35] and so the term size is used. The numbers given are based on measurements made by SEM and optical microscopy. The data show that the fibril widths appear to be nearly independent of the fiber "sizes" which vary by a factor of almost two among the different types of silkworms. The graph in Fig. 9 shows this more clearly. The correlation coefficient of the regression line is nearly equal to zero.

Student's *t*-test was applied to compare the geometric-mean fibril widths for the pairs of degummed fiber and peeled fiber of the same silk. The results show a 98% or greater probability that they are all different. The physical origin of these differences is not clear. Possibly, the sericin plays a role. Usually, a small amount remains on the fiber after degumming [48]. In any event, the peeled samples are of more interest since the interior fibrils, being much more numerous, presumably play a larger role in determining the physical properties of the fiber. Analysis with the *t*-test

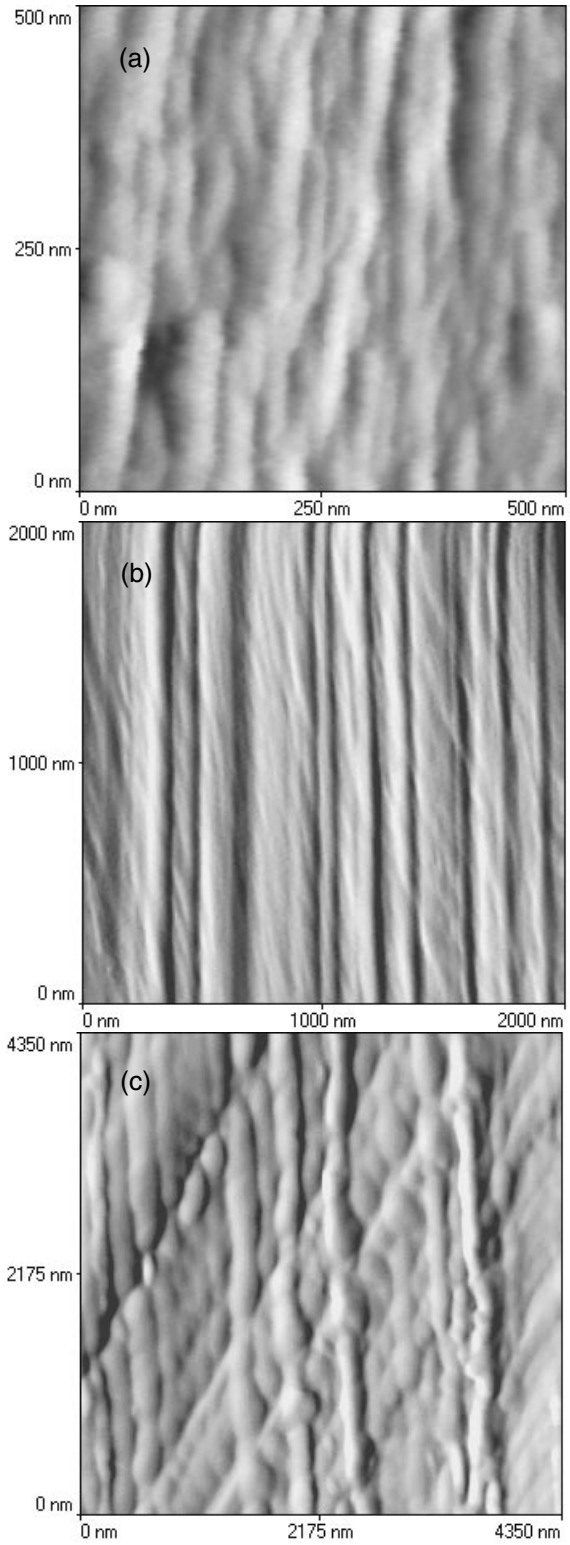

Fig. 3. AFM images of 4-molted *B. mori* silks revealing: (a) irregular nanofibrils; (b) bundles of nanofibrils and helical features; and (c) layered structure.

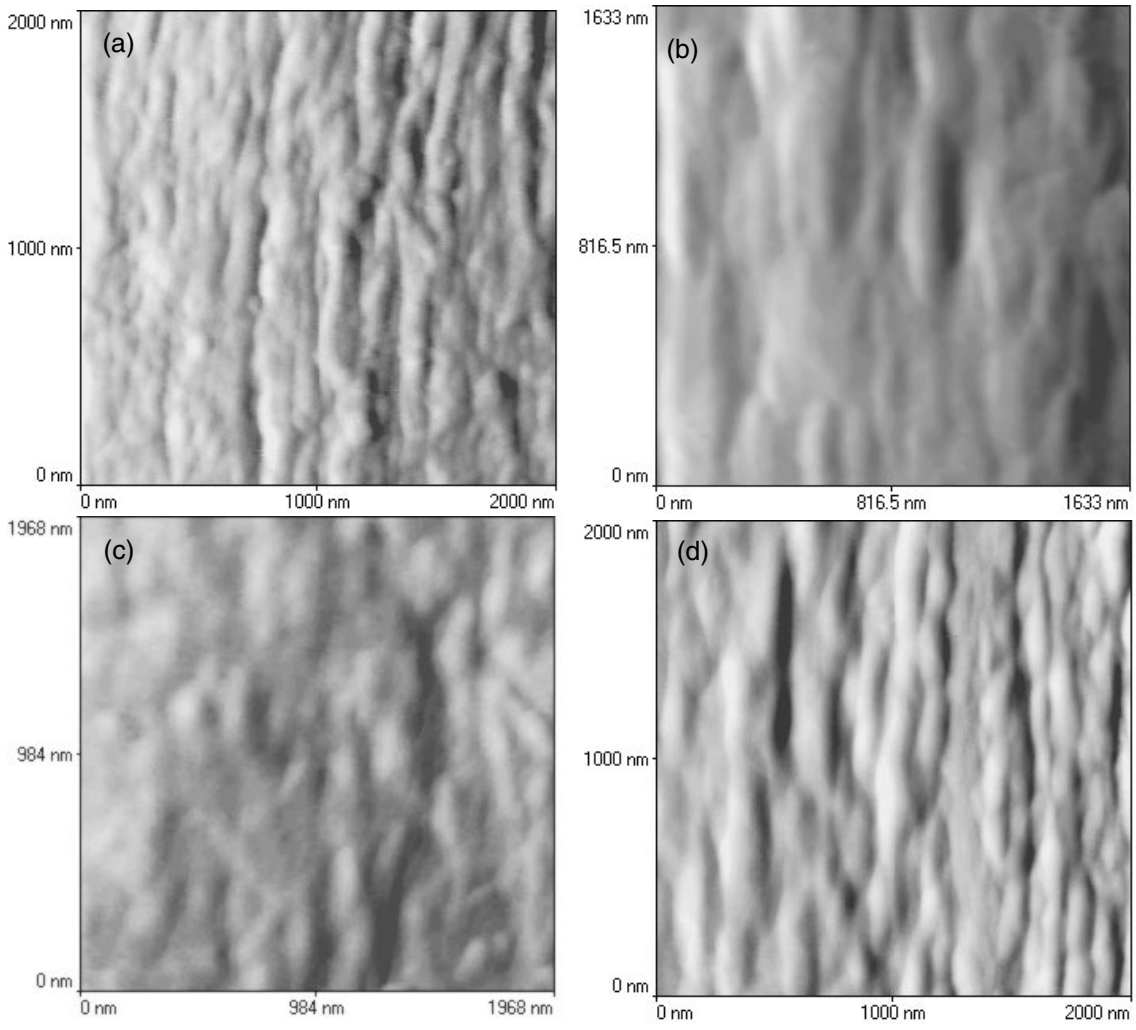

Fig. 4. AFM images of degummed silks: (a) *A. pernyi*; (b) *A. yamamai*; (c) sex-limited *B. mori*; and (d) 3-molted *B. mori*.

shows the geometric-mean fibril widths of peeled *A. yamamai* and peeled *A. pernyi* to be the same at a 65% probability and all the other possible pairs of peeled silks to be different at a 90% or greater probability level. The physical origin of these results also is not clear. The fibril formation mechanism must play a role in determining the width. Two possible mechanisms have been advanced for synthetic fibers, crystal nucleation and spinodal decomposition [49]. The former has been proposed as the dominant one for fibers of poly(*p*-phenylene benzo-bisthiazole) which, like silks, are formed from a liquid crystalline state [47,49]. A combination of the two mechanisms has been considered for

Table 1
Mean dimension and standard deviation of fibers and fibrils

Silk	Arithmetic mean fiber size (μm)	Fibril width (nm)			
		Arithmetic mean		Geometric mean	
		Degummed	Peeled	Degummed	Peeled
A. pernyi	21 ± 8	125 ± 56	130 ± 103	114 ± 2	109 ± 2
A. yamamai	16 ± 6	132 ± 82	134 ± 110	115 ± 2	110 ± 2
B. mori					
sex-limited, ♀	13 ± 3	181 ± 113	156 ± 86	153 ± 2	136 ± 2
4-molted	12 ± 2	120 ± 53	112 ± 82	110 ± 2	92 ± 2
3-molted	11 ± 4	119 ± 45	125 ± 85	111 ± 1	106 ± 2

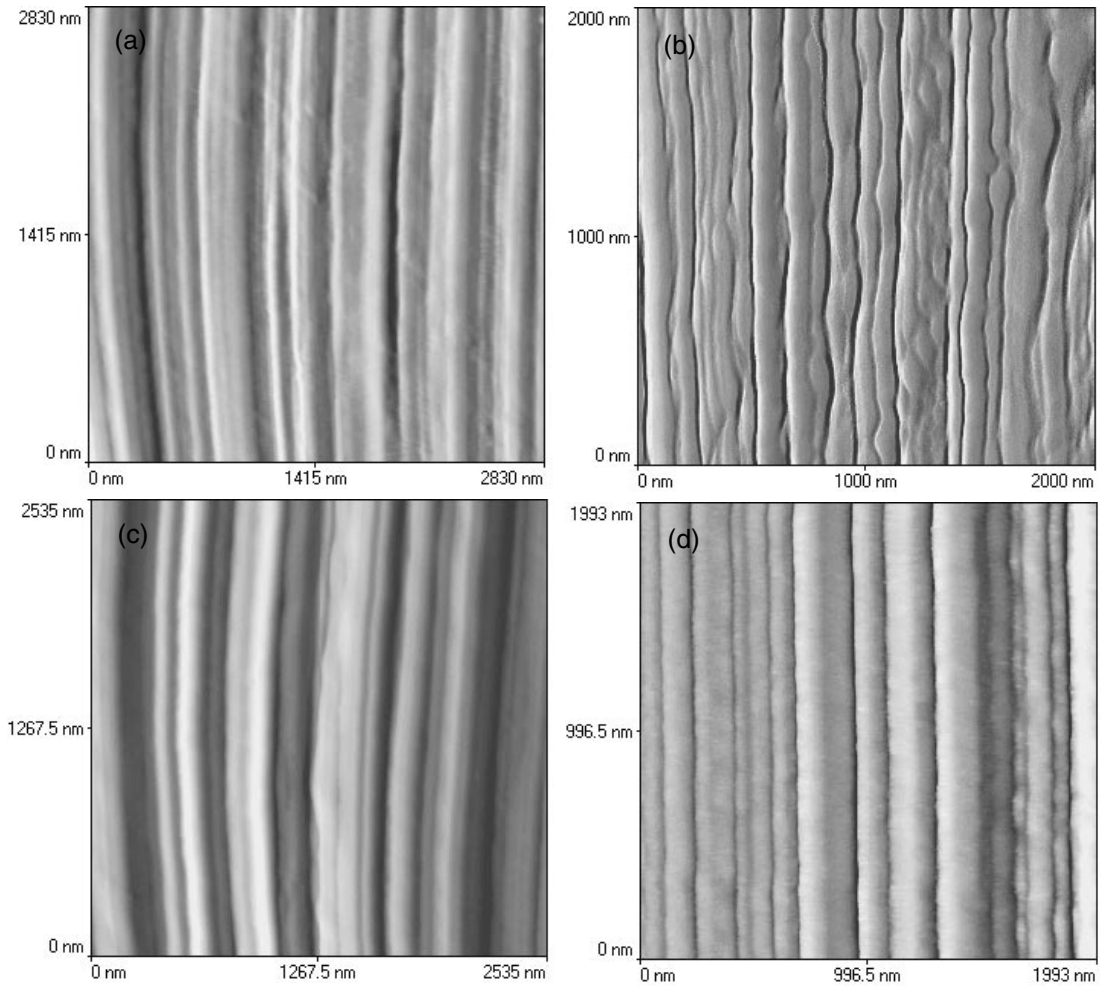

Fig. 5. AFM images of peeled silks revealing nanofibrils extended along the fiber axis: (a) *A. pernyi*; (b) *A. yamamai*; (c) sex-limited *B. mori*; and (d) 3-molted *B. mori*.

poly(*p*-phenylene terephthalamide) fibers which also are formed from a liquid crystalline state [50].

Table 2 shows the geometric-mean fibril width of peeled 4-molted *B. mori* as well as the arithmetic mean fiber size at the outside and inside of the single cocoon fiber as it is unwound from the cocoon. The result shows that the fibril width obtained from the outer portion is larger than the one from the inner portion. Since there is also a tendency of decreasing size of the fiber from the outer portion to the inner portion, there is a possible correlation of the change of size of fiber and width of fibril. According to Student's *t*-test the difference in fibril width is significant at 100% probability. However, it is not a large trend and the data fit rather well into the scatter in Fig. 9. If there is a trend, one possible reason for it is the change of gland content toward the end of the cocoon formation process. Another possibility is that the silkworm stretches the fiber in the inner portion of the cocoon more than that in the outer.

3.3. Cross angles

3.3.1. AFM data

Fig. 10 shows the distribution of cross angles from the peeled 4-molted *B. mori* silk. In general, the distributions

Table 2
Mean dimension and standard deviation of fiber and fibrils along the length of a single peeled fiber of 4-molted *B. mori*

Position on fiber	Arithmetic mean fiber size (μm)	Fibril width (nm)	
		Arithmetic mean	Geometric mean
Outer portion	11 ± 1	185 ± 80	170 ± 2
Inner portion	9 ± 2	130 ± 59	119 ± 2

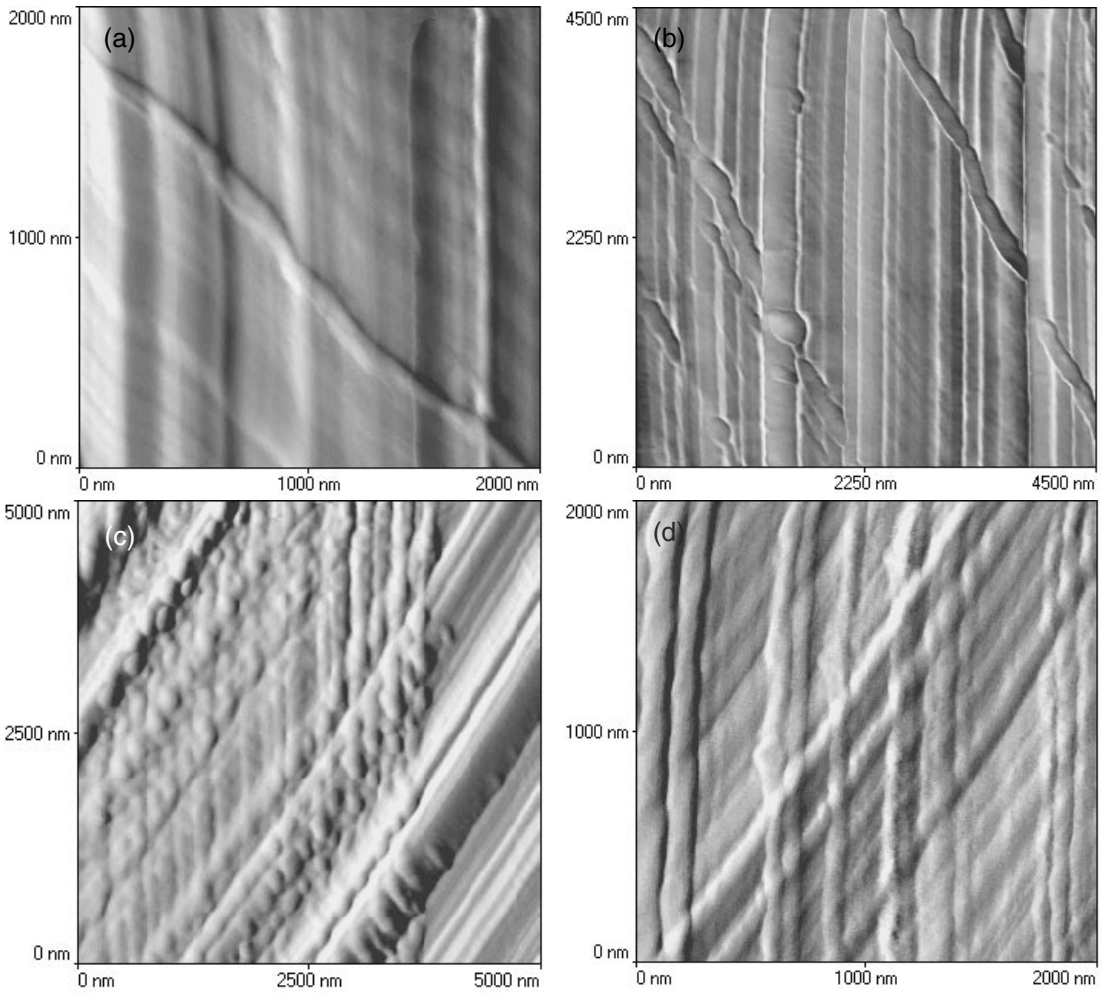

Fig. 6. AFM images of peeled silks revealing layered structures: (a) *A. pernyi*; (b) *A. yamamai*; (c) sex-limited *B. mori*; and (d) 3-molted *B. mori*.

are more nearly Gaussian than is the case for the widths. Again, the distributions are similar for all the other peeled silks as well as the degummed silks although the latter do not appear to exhibit a regularly layered structure [47]. The arithmetic mean of cross angles for all the silks are summarized in Table 3. They are in the range of 30–50°. While there is some correlation of the cross angle with the size of fiber (Fig. 11), there appears to be no

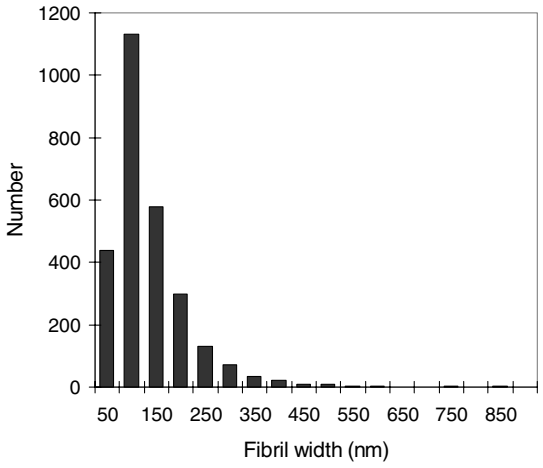

Fig. 7. Distribution of fibril widths in peeled 4-molted *B. mori* silk.

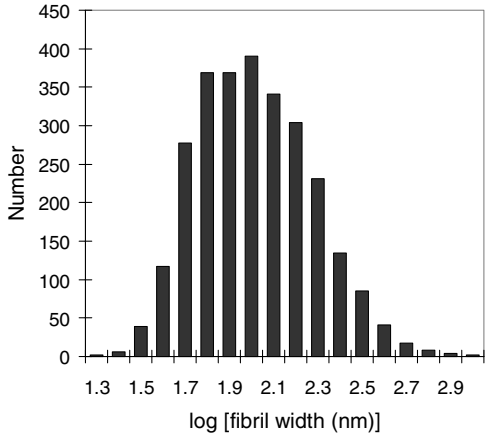

Fig. 8. Logarithmic distribution of fibril widths in peeled 4-molted *B. mori* silk.

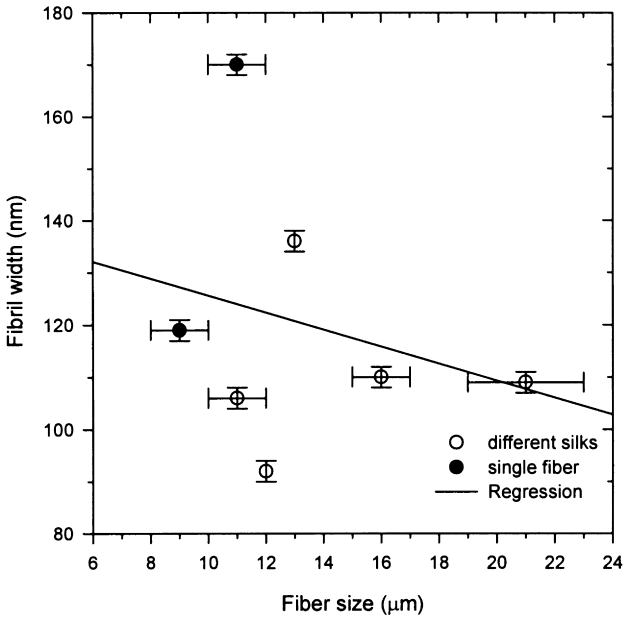

Fig. 9. Plot of geometric mean fibril width vs. arithmetic mean fiber size with the standard errors. The correlation coefficient is nearly equal to zero.

correlation of cross angle with the fibril width (Fig. 12). The correlation coefficients of regression for those two plots are 0.6 and 0, respectively.

Analysis with the *t*-test shows the cross angles of: degummed *A. pernyi* and degummed sex-limited *B. mori* (59%), degummed *A. yamamai* and degummed 4-molted *B. mori* (52%), degummed 4-molted *B. mori* and degummed 3-molted *B. mori* (51%) as well as peeled *A. yamamai* and peeled 3-molted *B. mori* (72%) to be the same at the given probabilities, and all the other possible pairs to be different at a 99% or greater probability level. The cross angles at the outside and inside of the single cocoon fiber as it is unwound from the cocoon of 4-molted *B. mori* are also shown in Table 3. The cross angles of the two parts are nearly the same regardless of the fiber size difference. The *t*-test shows

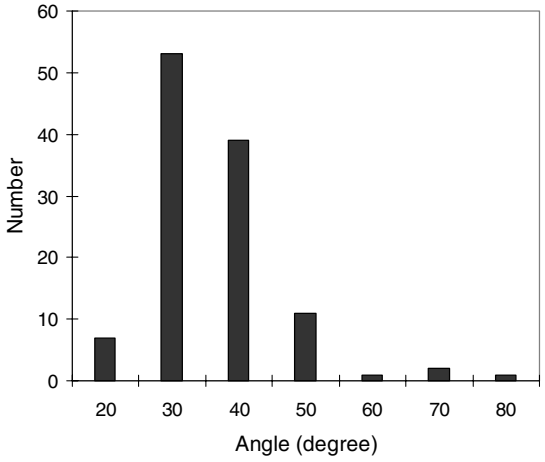

Fig. 10. Angular disribution of crossing fibrils in peeled 4-molted *B. mori* silk.

Table 3
Arithmetic-mean and standard deviation of cross angle of fibrils in different layers

Silk	Cross angle (degree)	
	Degummed silk	Peeled silk
A. pernyi	45 ± 10	48 ± 11
A. yamamai	38 ± 9	42 ± 15
B. mori		
sex-limited, ♀	44 ± 16	36 ± 11
4-molted	37 ± 9	31 ± 10
3-molted	35 ± 11	41 ± 13
4-molted outer portion	–	36 ± 8
4-molted inner portion	–	35 ± 10

them to be the same at 84% probability. The data fit relatively well with the data for different silks as shown in Fig. 11. If the angles for the larger fibers, *A. yamamai* and *A. pernyi*, (crystals are primarily alanine) are weighted with the inverse square of the standard deviation and averaged, the result is 46°. If the angles for the smaller fibers, various *B. mori*, (crystals are primarily alanine and glycine) are averaged in the same manner, the result is 36°. The mechanism that determines these angles is not known. There are at least two possibilities, both of which would be affected by the apparent variation of the cross angle with amino acid composition of the β-sheets. One might be the oriented nucleation of a new crystal on an existing one in the fibril below. Low-energy packings of β-sheets have been found over a range of angles for proteins [51] and at some angles for an α-helix on a β-sheet [52]. A somewhat related mechanism is the possible cross packing of the helical

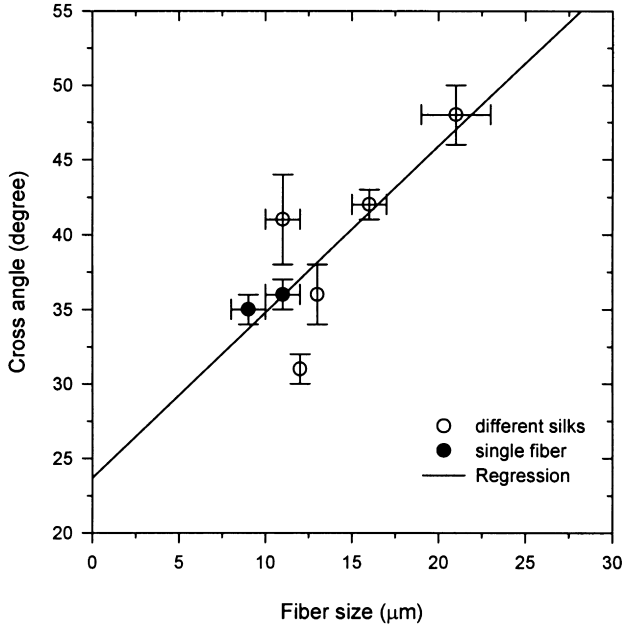

Fig. 11. Plot of cross angle vs. arithmetic mean fiber size with the standard errors. The correlation coefficient is 0.6.

Table 4
Parameters and standard deviations obtained for the azimuthal scan of *A. pernyi* fitted with three peaks

Parameter	Inner scan		Outer scan	
	Central peak	Offset peaks	Central peak	Offset peaks
A (counts)	630 ± 110	150 ± 130	650 ± 180	270 ± 20
n	37 ± 9	5 ± 7	34 ± 8	8 ± 3
φ_0 (°)	90	45 ± 11	90	45 ± 0.1
		135 ± 11		135 ± 0.1
Area	~ 405	~ 2(80)	~ 277	~ 2(74)
Percent of area in peaks	72	28	65	35

structures such as those in Figs. 3 and 4 as well as Refs. [33,34]. Such cross packing of helical structures governs the cross angles of globular proteins [53], isotactic polypropylene [54] and *B*-DNA [55] with the cross angle being twice the helix angle.

3.3.2. Wide angle X-ray diffraction

Details of the orientation distribution of the crystallites in the single fiber of *A. pernyi* were determined from the azimuthal spread of the two strong equatorial reflections, 200 (inner) and 120, 210 (outer) [40], on the normal incidence diffraction pattern. The intensity data, *I*, for both reflections were fit with a single peak of the form:

$$I = A \sin^n(\varphi)$$

Here, φ is the azimuthal angle. *A* is the amplitude of the peak and *n* is an integer, and both are adjustable parameters. The detector introduced some artifacts on the "right" side ($\varphi = 180 - 360$) and so only the data on the "left" side ($\varphi = 0 - 180$) were fit. The result is not too good at the peak and at the shoulders as shown by the dashed fitted lines in Fig. 13. Since the AFM images have shown fibrils aligned at three angles (−48, 0 and +48°) with respect to the fiber axis, an indication of this splitting was expected in the diffraction patterns as well. For this reason and in an attempt to improve the fit, the azimuthal scans through the maxima of both reflections were fitted with one central and two offset peaks. For each peak, φ was replaced by $(\varphi - \varphi_0 + \pi/2)$ where φ_0 is the angular location of the center of the peak. The quantities φ_0, *A* and *n* for the three peaks were adjusted for an optimum with the offset for the two offset peaks being kept equal. The results are shown in Table 4.

This yields a better, but not statistically significantly better, fit to the peak and shoulders as shown by a comparison of the solid (three peaks) and dashed (one peak) fitted lines in Fig. 13. The azimuthal scan through the outer peak would overlap the 201 peak, thereby complicating the situation. Therefore, the results for the scan through the inner peak are considered more meaningful. These initial data are consistent with about 72% of the crystals being parallel to the fiber axis, 14% at +45° to the axis and 14% at −45° to the axis. The total of the offset peaks, 28%, is in close agreement with the AFM result, 30%.

3.3.3. Modeling

With the EpiCalc software, no epitaxial angles were found in the range of the arithmetic mean cross angles observed with the AFM measurement. This indicates that the orientation is not due to "unit cell" epitaxy.

The excess energy calculated by molecular modeling for each orientation of the overlayer sheet with respect to the excess energy of the sheet oriented at 0° is given in Table 5. This arrangement of the sheet and crystal (0°), represents the most favorable way of packing. For structures I, II and IV, it represents perfect crystals. The results for the structures oriented initially at 15° are not given since the minimization process reoriented them to approximately the low energy zero orientation. In all other cases including the unconstrained crystal of Structure I, the final angle after minimization was within 0–6° of the starting angle with an average magnitude of the difference less than 2°. There are no strong minima in the excess energies except for the sheet overlayer

Table 5
Excess energy (kcal/mol) of packing β-sheets at different orientations

Orientation angle (°)	Excess energy (kcal/mol of overlayers)			
	Structure I	Structure II	Structure III	Structure IV
0	0	0	0	0
30	72	72	65	38
45	98	68	61	34
60	80	63	70	30
75	87	66	64	36
90	70	43	48	37

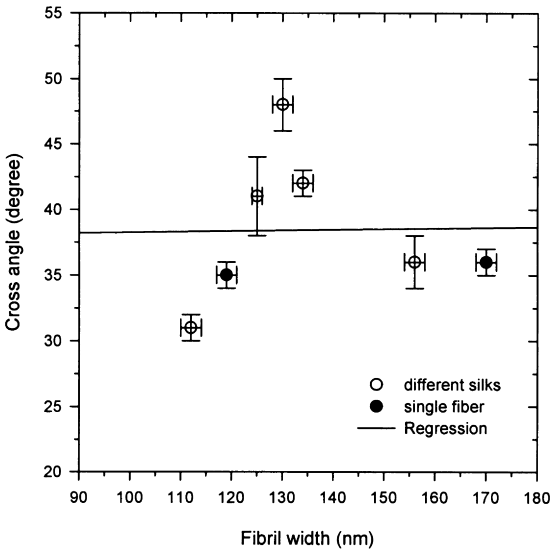

Fig. 12. Plot of cross angle vs. geometric mean fibril width with the standard errors.

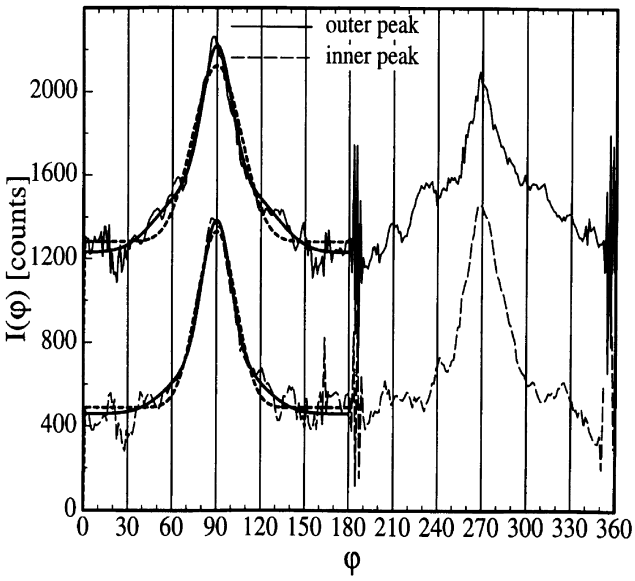

Fig. 13. The azimuthal scan fitted with a single peak (dashed line) and with three peaks (solid line).

oriented at 0°. In the angular range of 30–45°, corresponding to more than the range of observed cross angles of *B. mori*, the lowest energies are 72 at 30°, 68 at 45°, 61 at 45°, and 34 at 45° kcal/mol of overlayers for structures I–IV, respectively. From highest to lowest, these correspond approximately to 0.48–0.23 kcal/mol of backbone atoms or 32×10^{-3} to 15×10^{-3} J/m^2. While these numbers would allow the random attachment of some backbone atoms to the crystal, they alone do not establish the concept of growth of an oriented overlayer. The absence of a low energy minimum suggests that such an overgrowth probably does not occur. To answer the question more completely in the absence of a marked minimum requires the development of a detailed kinetic model of the nucleated overgrowth. There are a number of possible models all requiring the knowledge of a number of thermodynamic parameters. One model which illustrates this requirement for synthetic polymers is that for the kinetics of crystallization with chain folding [56]. The conclusion based on these initial calculations is that epitaxy at this scale does not occur for the flat sheets used in the model.

3.4. Some advantage of a nanofibrillar morphology

A multifibrillar fiber with weak bonding between fibrils offers a number of possible mechanical advantages over a solid fiber of the same total cross sectional area. One is that the fiber will have greater flexibility so that it requires a lower moment to bend through a given radius of curvature [57]. Another related advantage is that the fiber can be bent to a smaller minimum radius of curvature before failure occurs in tension on the outside of the bend or in compression on the inside of the bend [57]. Both of these are related to the fact that the shear involved in bending a solid fiber can be accommodated with little stress in the weakly bonded inter-fibril boundaries of a nanofibrillar fiber. The advantage concerning failure might be the explanation for the lack of failure in the dragline silk of *N. clavipes* under a very sharp bend [18,58].

Also it can be noted that if the crossing fibrils are arranged in a helical or zig-zag manner in the fiber, they could extend the strain to failure in tension and compression significantly. The former could occur because these non-straight fibrils would straighten parallel to the fiber as the originally “straight” ones extend and break. The latter could occur because the non-straight fibrils would compress in the manner of a spring as the “straight” ones undergo buckling or shear failure. Both effects could contribute to the lack of failure under a sharp bend noted above [18,58]. The tensile effect could contribute to the reported large tensile strains of spider silks at failure [59–61].

Finally it can be observed that if a void or other flaw is the size of the fibril diameter, only the fibril will fail. On the contrary, if the void were in a solid fiber which behaved in a brittle fashion, the whole fiber could fail at a critical stress [62].

3.5. Opportunities for future work

There are questions which remain. These provide a number of opportunities for future work. One is to resolve the formation mechanism for nanofibrils of silk. As noted, spinodal decomposition and/or crystal nucleation are likely candidates. A closely related opportunity is to determine the reason for the decrease of nanofibril width along a single cocoon fiber. It would be good to make measurements of fiber size and nanofibril width for the various types of silk so that the fibril width can be associated with the exactly corresponding fiber size for each silk. The mechanism governing the cross angle of the nanofibril also is unresolved. The cross packing of helical structures [53–55] could be examined in

more detail. In the present work, it has proven difficult to acquire a statistically adequate number of observations of the helix angles with sufficient accuracy to test the possibility.

4. Conclusions

The results presented here show that all silks studied exhibit nanofibrils. The log-normal distributions of fibril widths are similar for all silks. The geometric mean widths of nanofibrils cover the range of 90–170 nm and are independent of the fiber size from different types of silkworms. There is a layered structure with fibrils on different layers at a cross angle. The arithmetic mean cross angles are in the range of 30–50° depending on the silk. The cross fibrils are observed in 30% of the images. WAXD results are consistent with this number. Computer modeling revealed no epitaxy to account for the cross angles. It is proposed that the nanofibrils play a role in some of the attractive mechanical properties observed for silks. They are also relevant to some aspects of the structure. Opportunities for future work are indicated.

Acknowledgements

This work was supported by Technical Management Concepts, Inc. and NSF grant number 47.041. The authors thank Mr J Williams and Dr DW Tomlin of the Materials and Manufacturing Directorate, WPAFB as well as Mr D Hull of NASA Glenn Research for assistance with the LVHRSEM. Thanks to Dr GF Liu of the Zheijan Sichou Institute of Technology for providing some of the silks. Thanks to Dr J Magoshi of the National Institute of Agrobiological Resources and Dr Y Magoshi of the National Institute of Sericultural and Entomological Science, Japan who taught us how to reel and degum silks. Thanks to Dr RP Steiner of Akron for helpful discussion of statistical analysis. We thank Dr MD Ward of University of Minnesota for providing insight to his EpiCalc software. Finally, SP thanks the Ministry of Science, Technology and Energy, Thailand for a graduate scholarship.

References

[1] Marton L, Mcbain JW. Chemical Products 1942;July/August:1.
[2] Reneker DH. J Polym Sci 1965;A3:1069.
[3] Clark ES, Weeks JJ, Eby RK. In: French AD, Gardner KH, editors. Fiber diffraction methods, ACS Symposium Series 141Washington, DC: American Chemical Society, 1980. p. 183–92.
[4] Kambour RP. J Polym Sci 1966;4A2:399.
[5] Pennings AJ, Kiel AM. Kolloid Z Z Polym 1965;205:160.
[6] Keller A. J Polym Sci Polym Symp C 1977;58:395.
[7] Baumgarten PK. J Colloid Interface Sci 1971;36:71.
[8] Cohen Y, Thomas EL. Polym Engng Sci 1985;25(17):1093.
[9] Sawyer LC, Jaffe M. J Mater Sci 1986;21:1897.
[10] Schaper A, Zenke D, Schultz E, Hirte R, Taege M. Phys Status Solid A 1989;116:179.
[11] Kageyama K, Tamazawa J, Aida T. Science 1999;285:2113.
[12] Liu G, Ding J, Qiao L, Guo A, Dymov BP, Gleeson JT, Hashimoto T, Saijo K. Chem Eur J 1999;9:2740.
[13] Hock CW, McMurdie HF. J Res Natl Bur Stand 1943;31:229.
[14] Frey-Wyssling A, Muhlethaler K. Makromol Chem 1963;62:25.
[15] Engett AL, Carroll RJ. Leather Mfr 1965;82(8):29.
[16] Peters HM, Kovoor J. Zool J Physiol 1989;93:125.
[17] Stubbs DG, Tillinghast EK, Townley MA. Naturwissenschaften 1992;79:231.
[18] Mahoney DV, Vezie DL, Eby RK, Adams WW, Kaplan DL. In: Kaplan DL, Adams WW, Farmer BL, Viney C, editors. Silk polymers: materials science and biotechnology, ACS Symposium Series 544Washington, DC: American Chemical Society, 1994 (chap. 18).
[19] Miller LD, Putthanarat S, Eby RK, Adams WW. Int J Biol Macromol 1999;24:159.
[20] Kitagawa M, Kitayama T. Mater Sci 1997;32:2005.
[21] Li SFY, McGhie AJ, Tang SL. Biophys J 1994;66:1209.
[22] Vollrath F, Holtet T, Thøgersen HC, Frische S. Proc R Soc London, Ser B, Biol Sci 1996;263(1367):147.
[23] Zarkoob S, Reneker DH, Eby RK, Hudson SD, Ertley D, Adams WW. Polym Prepr 1998;39(2):244.
[24] Zahn H. Kolloid Z 1949;112:91.
[25] Hegetschweiler R. Makromol Chem 1950;4:156.
[26] Marsh RE, Corey RB, Pauling L. Biochim Biophys Acta 1955;16:1.
[27] Dobb MG, Fraser RDB, Macrae TP. J Cell Biol 1967;32:289.
[28] Mercer EH. Aust J Sci Res B 1952;5(3):366.
[29] Yamaura K, Okumura Y, Ozaki A, Matsuzawa S. J Appl Polym Sci, Polym Symp 1985;41:205.
[30] Tsubouchi K. Farming Jpn 1996;30-5:36.
[31] Freddi G, Gotoh Y, Mori T, Tsutsui I, Tsukada M. J Appl Polym Sci 1994;52:775.
[32] Lotz B, Gonthier-Vassal A, Brack A, Magoshi J. J Mol Biol 1982;156:345.
[33] Putthanarat S. MS thesis, The University of Akron, 1995.
[34] Putthanarat S, Eby RK, Adams WW, Liu GF. J M S Pure Appl Chem A 1996;33(7):899.
[35] Iizuka E. Biorheology 1965;3:1.
[36] Hillier AC, Ward MD. Phys Rev B 1996;54(19):14 037.
[37] Cramer E. J Prakt Chem 1865;96:76.
[38] Putthanarat S, Eby RK, Gurke I, Stribeck N. Hasylab Annu Rep 1998;1:723.
[39] Marsh RE, Corey RB, Pauling L. Biochim Biophys Acta 1955;16:1.
[40] Warwicker JO. J Mol Biol 1960;2:350.
[41] Fraser RDB, MacRae TP. Conformation in fibrous proteins and related synthetic polypeptides. New York: Academic Press, 1973 (chap. 13).
[42] Cammarata RC. Surf Sci 1992;279:341.
[43] Urs RG, Subramanya G, Somashekar R. Textile Res J 1993;63(10):610.
[44] Somashekar R, Urs RG. Polymer 1993;34(13):2711.
[45] Takahashi Y, Gehoh M, Yuzurika K. J Polym Sci Polym Phys 1991;29:889.
[46] Salemme FR. Proc Biophys Mol Biol 1983;42:95.
[47] Putthanarat S. PhD dissertation, The University of Akron, 1999.
[48] Krasowski A, Mueller B, Foehles J, Hoecker H. Melliand Textilberichte 1999;80:543 (see also p. E144).
[49] Cohen Y, Thomas EL. Polym Engng Sci 1985;25(17):1093.
[50] Wang W, Ruland W, Cohen Y. Acta Polym 1993;44:273.
[51] Chou KC, N'emethy G, Rumsey S, Tuttle RW, Scheraga HA. J Mol Biol 1986;188:641.
[52] Chou KC, N'emethy G, Rumsey S, Tuttle RW, Scheraga HA. J Mol Biol 1985;186:591.
[53] Chothia C, Levitt M, Richardson D. J Mol Biol 1981;145:215.
[54] Lotz B, Wittman JC. J Polym Phys 1986;24B:1541.
[55] Timsit Y, Moras D. J Mol Biol 1991;221:919.

[56] Hoffman JD, Miller RL. Polymer 1997;38:3151.
[57] Hull D. An introduction to composite materials. Cambridge: Cambridge University press, 1995 (chap. 2 and 3).
[58] Cunniff PM, Fossey SA, Aurbach MA, Song JW, Adams WW, Eby RK, Mahoney D, Vezie DL. Polym Adv Technol 1994;5:401.
[59] Zemlin JC. A study of the mechanical behavior of spider silks. Technical report 69-29-CM to the US Army Natick Laboratories, Collaborate Research Inc., September 1968.
[60] Butterworth GAM, Leny RW. The tensile properties of spider silk. Final report C65593 to US Army Natick Laboratory, Fabric Research Laboratories, Dedham, MA, May 1996.
[61] Kaplan D, Lombardi SJ, Muller W, Fossey S. In: Byron D, editor. Biomaterials from biological sources, New Jersey: Stockton, 1991.
[62] Hull D. An introduction to composite materials. Cambridge: Cambridge University Press, 1995 (chap. 3).